

Effects of Impurities on the Biodegradation Behavior of Pure Magnesium

Ji-Young Lee^{1,2}, Gilsoo Han³, Yu-Chan Kim¹, Ji-Young Byun¹, Jae-il Jang²,
Hyun-Kwang Seok¹, and Seok-Jo Yang^{4,*}

¹Division of materials, Korea Institute of Science & Technology, Seoul 136-650, Korea

²Division of Materials Science and Engineering, Hanyang University, Seoul 133-791, Korea

³Division of Non-ferrous Refining Project,
Research Institute of Industrial Science & Technology,
Pohang-si, Gyeongbuk 790-600, Korea

⁴Department of Mechatronics Engineering, Chungnam National University,
Daejeon 305-764, Korea

(received date: 28 January 2009 / accepted date: 21 May 2009)

The corrosion behavior of pure magnesium that has different content ratio of impurities (such as Fe/Mn ratio) in Hanks' solution was investigated in order to tailor the lifetime of biodegradable implant made of pure magnesium. Two distinct stages of corrosion were observed: a slow corrosion rate stage and a subsequent fast corrosion rate stage. The first stage was characterized by uniform corrosion that produced magnesium hydroxide and calcium phosphate film on a magnesium surface, resulting in a slow corrosion rate. The second stage with an abrupt increase in the corrosion rate was induced by Fe precipitates and was stimulated by an increase in the Fe/Mn ratio. This corrosion was developed to a preferred crystallographic pitting corrosion where the pits propagated along the preferred crystallographic plane and several layers of Mg planes with narrow interplanar space remained uncorroded. From this study, it is expected that the lifetime of the biodegradable implant made of pure Mg can be tailored by controlling the amount and ratio of the impurities.

Keywords: pure magnesium, corrosion, biodegradation, impurity effect, preferred crystallographic pitting corrosion

1. INTRODUCTION

Several million people suffer from bone fractures annually and the growth rate of the bone fracture cases has been increasing drastically because of more vigorous sport activities, social instability, traffic accidents, and a prolonged human life. Many of these fractures are so complex for external medical treatment that they have to be surgically fixated by internal bone implants. Traditional surgical fixations have been executed by using permanent metal implants, such as bone screws, bone plates, and spinal instruments made of steel or titanium alloys. However, these internal fixations that use metallic materials have several disadvantages. Conventional metal implant materials, including Ti alloys, stainless steels, and Co-Cr alloys have too high Young's modulus (about 100 GPa to 200 GPa), which is much higher than that of cortical bone (~20 GPa). This mismatch makes the natural bone unable to bear external stress, which is referred to as "stress shielding," resulting in the

self-weakening of the bone [1]. Furthermore, additional surgical intervention is often required in order to remove metal implants 1 or 2 years after operation as the implant can cause physical irritation and chronic inflammatory reactions which can lead to the anguish of patient, the drudgery of the surgeon, the risk of medical accidents, and social and economical cost [2-4].

To overcome these drawbacks of the conventional inert metal implants, biodegradable implants, which bear stress temporarily during tissue recovery and gradually dissolve into the body afterwards, are of special interest for medical applications [5]. Currently, most of the biodegradable implants are made of polymers, such as Polylactic Acids (PLA), Polyglycolic Acid (PGA), or copolymer (PLDA). However, these bio-degradable polymers have relatively low strength and an unpredictable degradation rate, which can result in a sudden collapse of the implant during degradation in a living body [3,4]. In addition, the biodegradable polymer decreases the pH value of body fluids when it dissolves in a living body, which is not desirable for the promotion of bone growth [6]. For these reasons, the usage of biodegradable polymers is very limited.

*Corresponding author: sjyang@cnu.ac.kr

Recently, Mg and Mg alloys have been getting more interest in medical science as biodegradable materials because of their elastic modulus and compressive yield strength that are similar to those of natural bone, their excellent biocompatibility, and other positive effects they have on the growth of new bone during the biodegradation process [7-9]. Due to these advantages, Mg alloys are considered to be promising candidate materials for biodegradable orthopedic implants, vascular stents, bone grafts, and scaffolds for bone ingrowths [10,11]. Nowadays, there are many possibilities to tailor the biodegradation rate and mechanical strength of Mg alloys by changing the composition of alloying elements and improving the metallurgical process [7,10,12-15]. However, some alloying elements can cause a high risk of unexpected side effects during in vivo service. Thus, pure Mg can be applied to some biodegradable implants that require relatively low strength and a relatively slow degradation rate without any anxiety about the side effects from alloying elements. With this in mind, in this study, the corrosion mechanism of pure Mg in Hanks' solution and the effects of trace impurities on the corrosion of pure Mg were investigated to tailor the biodegradation rate.

2. EXPERIMENTAL PROCEDURE

2.1. Materials and sample preparation

Three different commercial pure Mg ingots were used in this study. The sample was prepared by melting and casting the pure Mg ingots under an Ar atmosphere in a vacuum and inert gas atmosphere furnace. Before the Ar gas was put into the furnace, the oxygen and moisture in the furnace were removed by using a vacuum to 10^{-3} torr at room temperature. The temperature of a STS430 steel crucible was filled with the pure Mg and was kept at 720 °C for 90 min in order to melt the Mg completely. Then, the molten Mg was stirred for 5 min. Afterwards, the molten Mg was casted into a STS430 steel mold and was cooled down in the same furnace. After casting, a specimen of rectangular parallelepiped of size $10 \times 20 \times 60 \text{ mm}^3$ was prepared by cutting the as-cast ingot along a longitudinal direction. The chemical compositions of the specimens were determined by Inductively Coupled Plasma (ICP, ARIAN 710-ES) analysis and are shown in Table 1. The specimen was cut into plate samples with $10 \times 10 \times 1 \text{ mm}^3$ for the immersion test and the samples were abraded with SiC emery paper of 800 grits, 1200 grits, and

Table 1. Chemical composition (wt.%) and Fe/Mn ratio of pure magnesium samples

Sample	Fe	Ni	Al	Mn	Fe/Mn
Sample #1	0.0014	0.0020	0.0021	0.0015	0.933
Sample #2	0.0092	0.0027	0.0043	0.038	0.242
Sample #3	0.0214	0.0027	0.0053	0.0036	5.944

Table 2. Chemical composition of Hanks' solution

Compound	Molecular weight (g/mol)	Mass (g/L)
$\text{KH}_2\text{PO}_4 \cdot \text{H}_2\text{O}$	136.09	0.060
$\text{Na}_2\text{HPO}_4 \cdot 2\text{H}_2\text{O}$	178	0.060
NaCl	58.44	8.000
KCl	74.55	0.400
NaHCO_3	84.01	0.350
$\text{MgSO}_4 \cdot 7\text{H}_2\text{O}$	246.47	0.200
Glucose	180.16	1.000
$\text{CaCl}_2 \cdot 2\text{H}_2\text{O}$	147.02	0.185

2000 grits. After abrading, each sample was degreased and cleaned in ethanol using an ultrasonic cleaner.

2.2. Immersion test

For the immersion test, was used Hanks' solution whose composition is listed in Table 2. Before the test, the pH value of the solution was adjusted to 7.4 by adding a dilute NaOH or HCl solution.

Seven Mg plate samples with a total area of around 28 cm^2 were hung in a sample holder and were then immersed in 1 L of Hanks' solution at room temperature. The corrosion rate of the samples was estimated by measuring the amount of generated hydrogen by using a funnel, as shown in Fig. 1. The adhered hydrogen bubbles on the surface of the sample and funnel were separated by periodical external vibration that was applied during the immersion test in order to obtain precise data. After the immersion test, the corrosion morphology and corrosion products were analyzed by a Scanning Electron Microscopy (SEM, HITACHI S4200) with a Wavelength Dispersive X-ray Spectroscopy (WDS, JEOL JXA-8500F) and an Energy Dispersive X-ray Spectroscopy (EDS, HITACHI S4200).

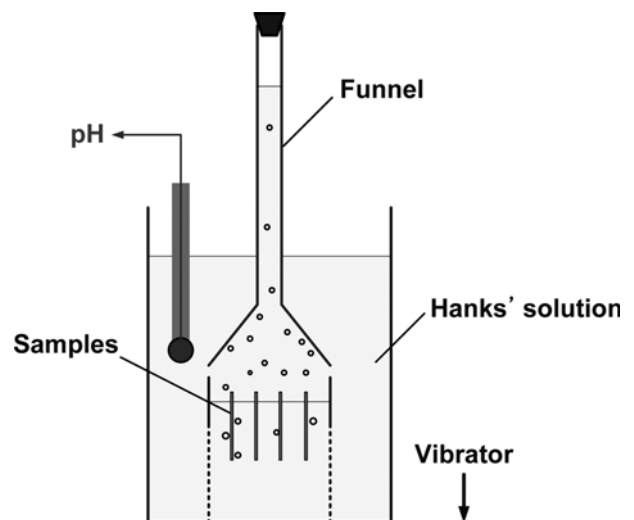
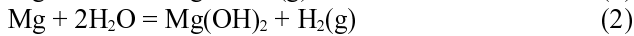
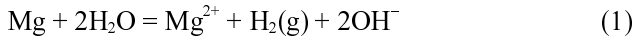


Fig. 1. Schematic diagram for immersion test setup.

3. RESULTS

3.1. Measurement of corrosion amount

The corrosion amount of a pure Mg sample was evaluated by measuring the amount of hydrogen evolution during the immersion test because Mg is generally corroded by reactions with water to form gaseous hydrogen. The possible overall reactions between water and Mg can be represented by:



The reactions indicate that one mole of H_2 gas is generated by the reaction of one mole of Mg. Thus, the corrosion amount of Mg that was measured by hydrogen evolution is reliable.

The amount of hydrogen evolution for the three different pure Mg samples (#1 ~ #3 in Table 1) as a function of immersion time in Hanks' solution is shown in Fig. 2. It was obvious that the corrosion behavior of each sample was quite different. In the case of Sample #1, the corrosion process consisted of two distinct stages: 1) the initial slow corrosion rate stage and 2) the subsequent fast corrosion rate stage. However, Sample #2 did not have the second stage in the immersion time of 190 h and Sample #3 had a very short period of the first stage. This dissimilarity in the corrosion behavior of the pure Mg samples may have been caused by the difference in impurity contents between the samples (see Table 1). The difference in the Fe and Mn concentration between the samples was significant, whereas that in Ni and Al was relatively small. Thus, the Fe and Mn had a strong influence on the difference in the corrosion behavior of the samples.

During the first stage, slow hydrogen evolution occurred evenly on the surface of the samples, implying that the samples were uniformly corroded. Sometimes hydrogen gas was

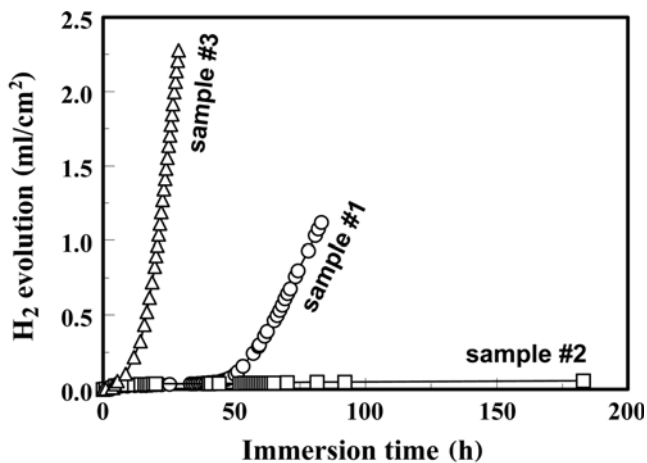


Fig. 2. Immersion test results for three different pure Mg samples as a function of immersion time in Hanks' solution.

locally generated, but this localized corrosion reaction disappeared shortly. When the corrosion process entered the second stage, fast and localized hydrogen evolution was observed and this reaction continued, suggesting that localized corrosion, such as pitting, might have occurred during this stage.

3.2. Microstructure of corrosion products

Figure 3 shows the microstructure of the corrosion products on the surface of the corroded samples on the first stage. All the samples were covered with corrosion product film and flower-like corrosion products were locally formed on the surface (see Fig. 3(a)). These two types of corrosion products were composed of magnesium, oxygen, calcium, and phosphorus, indicating that calcium ion and phosphorus

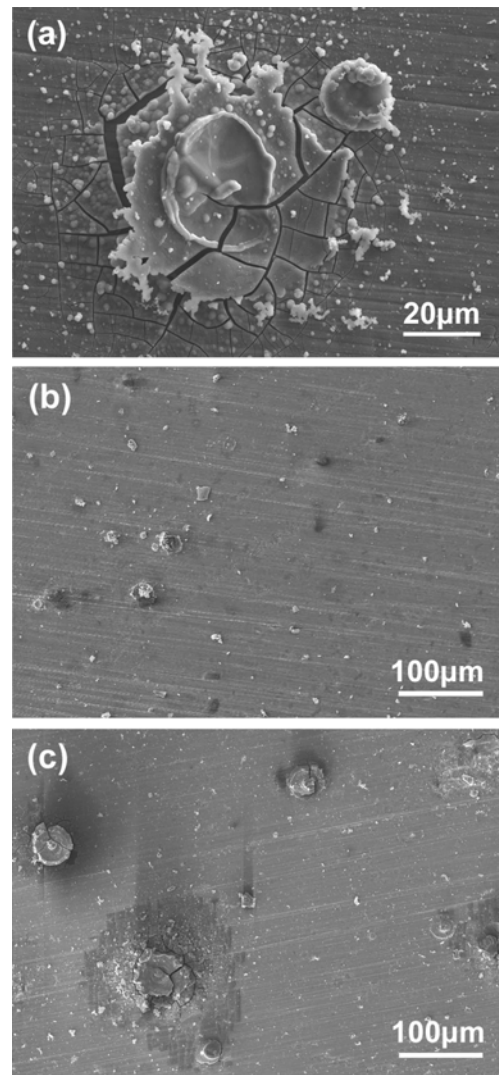


Fig. 3. SEM micrographs for the corrosion products on the surface of three different pure Mg on the first stage: (a) sample #1 for an immersion time of 50 h; (b) sample #2 for an immersion time of 180 h; (c) sample #3 for an immersion time of 10 h.

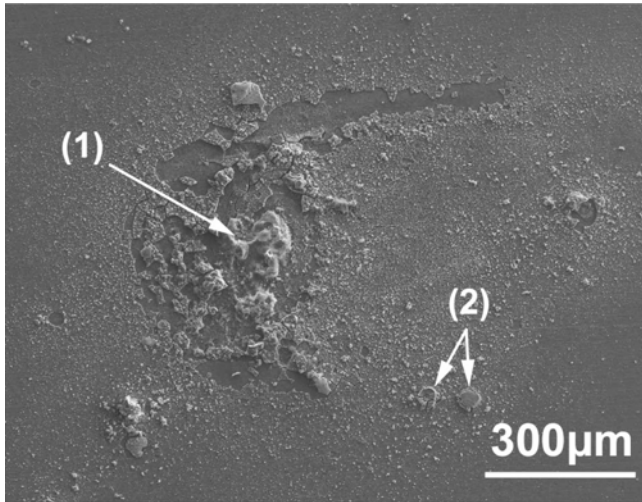


Fig. 4. SEM micrographs of the corroded surface on the intermediate stage between the first and the second stage: (1) activated area and (2) suppressed area.

ion in the solution were involved in the reaction on the surface of pure Mg. From this, it is expected that the corrosion products are calcium phosphate that contains magnesium or magnesium hydroxide. While the flower-like products on Samples #1 and #3 were well developed, those on Sample #2 were not (see Fig. 3), even though the immersion time of Sample #2 was much longer than those of the others. The site with flower-like corrosion products can be considered an area where corrosion reaction occurred more severely than the other place. In other words, localized corrosion occurred where there were flower-like corrosion products. This localized corrosion is believed to be responsible for the localized hydrogen evolution that occurred during the first stage, as mentioned earlier.

As the corrosion progressed, some of the localized corrosion sites became enlarged and some of them became suppressed as shown in Fig. 4. This enlarged corrosion site was developed to an activated area where the hydrogen evolution rate or corrosion rate increased abruptly to shift the first stage to the second stage. Thus, Sample #2, which did not suffer from the second stage corrosion, did not have any activated site under the conditions of this study. It was of interest that a special type of pitting corrosion was discovered on the second stage: The corrosion progressed along a preferred crystallographic plane and several layers of Mg planes with a narrow interplanar space remained uncorroded, as shown in Fig. 5. This corrosion resulted in an enormous increase in the surface area for reactions, and thus, the corrosion rate was abnormally increased. This type of corrosion will be named Preferred Crystallographic Pitting (PCP) corrosion because of the preferred direction of the pits' propagation.

In order to investigate this localized corrosion, the flower-

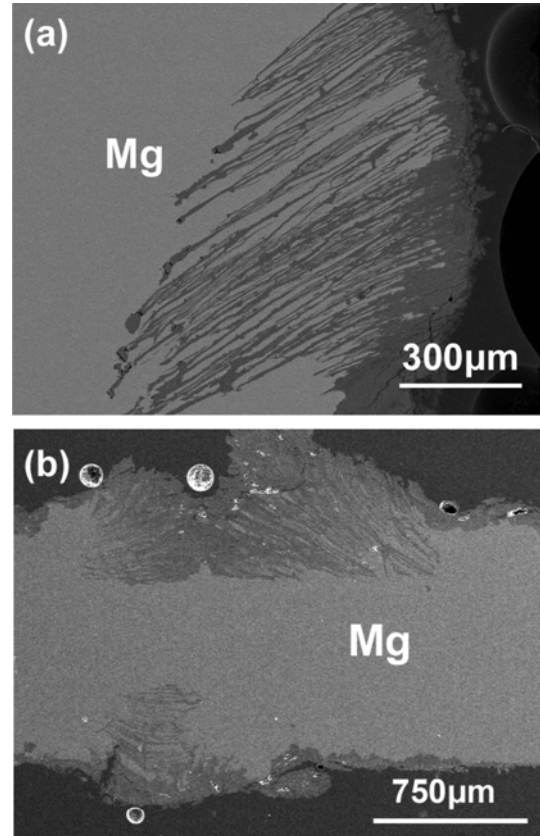


Fig. 5. SEM micrographs of the cross-section of pure Mg on the second stage: (a) sample #1 for an immersion time of 50 h and (b) sample #3 for an immersion time of 10 h.

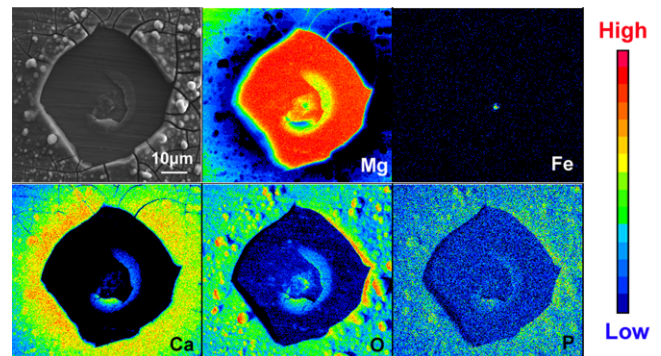


Fig. 6. Microstructure and WDS element mapping analysis of locally corroded area of sample #1 after removing the flower-like corrosion product.

like product was removed from the surface in order to conduct the element analysis by means of WDS mapping (see Fig. 6). According to the mapping analysis, the Mg matrix is beneath the flower-like product and the Fe element is located at the center of the exposed Mg matrix, indicating the Fe precipitate may have played a decisive role in the localized intensive corrosion of pure Mg. This effect of Fe on the corrosion behavior is believed to be due to the galvanic corro-

sion between the Mg matrix and the Fe precipitate: Corrosion potential of Fe is much higher than that of Mg, and thus, the Fe precipitates provide active cathodic sites and the Mg near Fe precipitates acts as an anodic site [16,17]. Since Fe has almost no solubility in solid Mg, the impurity Fe is segregated to form pure Fe precipitates during the solidification. In this respect, it can be expected that the corrosion rate will increase as the concentration of Fe increases. However, the corrosion rate of Sample #2 was much slower than that of Sample #1 because of the absence of the enlarged corrosion site as an activated site, even though Sample #2 had a higher content of Fe impurity than Sample #1. According to previous studies on the impurity effects on the corrosion of Mg [18,19], Mn can improve the corrosion resistance of Mg that contains harmful elements, such as Fe, Ni, and Cu. It has been suggested [20] that the Fe/Mn ratio, rather than the absolute content of Fe, was a critical factor that determined corrosion behavior. This ratio for each sample is summarized in Table 1. The order of the Fe/Mn ratio for the samples (Sample #3 > Sample #1 > Sample #2) is the same as that of the corrosion rate. Thus, the Fe/Mn ratio can be applied as the critical factor to pure Mg with trace amount of impurities. The possible mechanism of the Mn effect on the corrosion resistance is that Mn encapsulates the Fe particles during solidification due to a high affinity of Mn to Fe, and thereafter, the encapsulated particle becomes a less active cathodic site than the pure Fe precipitate [19]. This is due to the fact that the corrosion potential difference between Mn and Mg is smaller than that between Fe and Mg. This smaller corrosion potential difference leads to a slower hydrogen evolution on the cathodic site, which results in a high possibility of passivation induced by the corrosion products because the gaseous phase evolution on the surface hinders the formation of solid products on the same surface. Therefore, as the content of Mn increases, the period of the first stage increases and the localized intensive corrosion around Fe precipitates is inhibited.

When the localized corrosion around the Fe precipitates is enhanced by an undefined localized corrosive condition, the PCP corrosion can be initiated and the pits are propagated along a preferred direction. To our best knowledge, this extraordinary corrosion phenomenon of pure Mg in aqueous solution has not been reported in previous studies. Although the mechanism of the PCP corrosion phenomenon is not fully understood yet, it is clear that this new type of corrosion takes place around Fe precipitates. For more detailed investigation of this phenomenon, the composing elements around the PCP corrosion area were characterized by WDS mapping, and the result is shown in Fig. 7. One can see in the figure that excessive chlorine exists in the pits along the preferred crystallographic plane, which results from the induced acidic environment in the pits, and hence, accelerates the corrosion rate of metal.

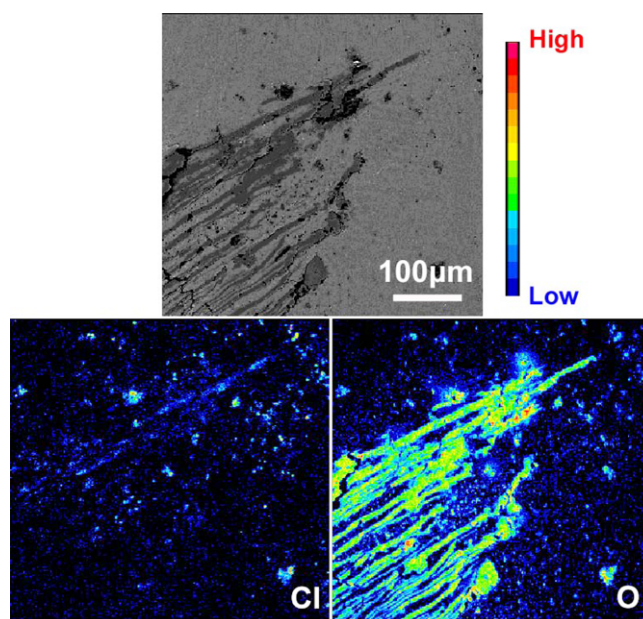


Fig. 7. Microstructure and WDS element mapping analysis of PCP corrosion of sample #1.

4. DISCUSSION

Since there are two distinct stages in the corrosion process of pure Mg in the Hanks' solution, it is expected that the mechanisms of the two stages are different. The characteristics of the first-stage corrosion are slow hydrogen evolution and uniform formation of solid corrosion products on the surface. As discussed earlier, the corrosion products in this stage was magnesium hydroxide and calcium phosphate. Figure 8(a) schematically illustrates a proposed corrosion mechanism for the first stage that may be characterized as a uniform attack, localized galvanic corrosion, and subsequent passivation by the formation of magnesium hydroxide and calcium phosphate.

When the pure Mg was exposed to the Hanks' solution with a pH value of 7.4, the forward reaction of Eq. 1 was thermodynamically stable to dissolve Mg as a form of Mg^{2+} and increase the pH value of the solution adjacent to the surface. Above a certain pH value, the stable phase changed to $Mg(OH)_2$ or calcium phosphate, such as hydroxyapatite, which is represented by the forward reactions of the following chemical equations:



These solid products uniformly covered the surface of the Mg sample, resulting in a slow corrosion rate. In addition, as mentioned earlier, galvanic coupling between the Fe precipitates and Mg matrix led to localized corrosion, which produced flower-like calcium phosphate (see Fig. 3). Most of

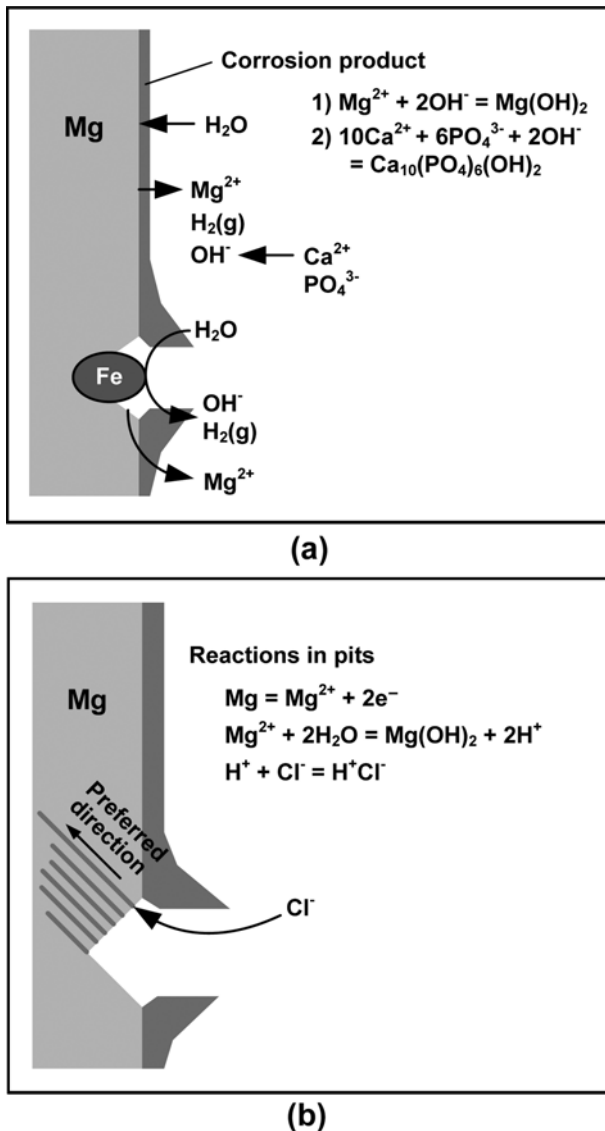
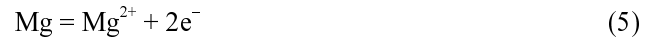


Fig. 8. Corrosion mechanisms for (a) the first stage and (b) the second stage.

the sites for this localized corrosion were passivated by covering the localized area with the flower-like solid product, causing this localized corrosion reaction on the first stage to be restrained after a short period of reaction.

Based on the results of the hydrogen evolution and microstructure, the mechanism of the second stage is presented in Fig. 8(b), which can be characterized by the PCP corrosion that abruptly increased the corrosion rate. At the beginning of the second stage, some of the Fe precipitates continuously acted as local cathodes while the surrounding Mg was intensely corroded in order for the pits to be developed under an undetermined condition. The pits propagated according to the following reactions, which are the anodic reaction of Mg and another form of reaction from Eq. 3.



while hydrogen evolution occurred at the cathodic sites. As the pits propagated, the solution in the pits was positively charged due to the excess hydrogen ion in Eq. 6. To neutralize the solution with this excess positive charge, anions in the bulk solution needed to migrate into the pits. Since chloride ion was the anion with the highest diffusivity in the solution, the chloride ions could diffuse into the pits, resulting in the chlorine element appearing in the pits, as shown in Fig. 7. The concentrated chloride ions resulted in the formation of a HCl environment in the pits and consequently accelerated the pit propagation, that is, the corrosion reaction of pure Mg. An interesting feature of this pitting corrosion is that the pits were propagated along a preferred crystallographic plane and layers of uncorroded plane were parallel to a certain plane. Since the interplanar space was narrow, the area of the reaction surface increased rapidly as the pit propagation progressed, resulting in an enormous corrosion rate.

The reason for this preferred crystallographic pitting corrosion of pure Mg is not clear, but that of other Hexagonal Closed-Packed (HCP) structured metal, such as beryllium and zinc, has been studied by Lillard *et al.* [21]. They suggested that the preferred crystallographic pits in beryllium and zinc were determined by metal-metal bonding strength that was dependent on the crystallographic orientation. Thus, it is valuable to apply their suggestion to this pure Mg corrosion in future studies.

5. CONCLUSIONS

The corrosion of pure Mg in Hanks' solution consisted of two consecutive stages: a slow corrosion rate stage and a subsequent fast corrosion rate stage. The corrosion behavior was dependent on the content ratio of impurities, such as Fe/Mn ratio, rather than the content value of them. As the Fe/Mn ratio increased, the period for the first stage became shortened. During the first stage, the Mg surface was covered with a film of magnesium hydroxide and calcium phosphate, resulting in a slow corrosion rate. The abrupt corrosion in the second stage was stimulated by Fe precipitates and was caused by Preferred Crystallographic Pitting (PCP) corrosion that produced layers of uncorroded planes with a narrow interplanar space. From these results, it can be expected that the lifetime of biodegradable implants made of pure Mg can be tailored by controlling the amounts and relative ratio of Fe and Mn.

ACKNOWLEDGMENTS

The authors would like to acknowledge the foundation of KIST project (Project #; 2E21410), R&D Program for Core

Technology of Materials (Project #; K0006028), and U&I Corporation for their support of this work.

REFERENCES

1. J. Nagels, M. Stokdijk, and P. M. Rozing, *J. Shoulder Elb. Surg.* **12**, 35 (2003).
2. G. Mani, M. D. Feldman, D. Patel, and C. M. Agrawal, *Biomaterials* **28**, 1689 (2007).
3. G. O. Hofmann, *Arch. Orthop. Traum. Su.* **114**, 123 (1995).
4. L. Claes and A. Ignatius, *Der chirurg* **73**, 990 (2002).
5. J. Levesque, D. Dube, M. Fiset, and D. Mantovani, *Adv. Mater. Process* **162**, 45 (2004).
6. O. Böstman and H. Pihlajamäki, *Biomaterials* **21**, 2615 (2000).
7. Z. Li, X. Gu, S. Lou, and Y. Zheng, *Biomaterials* **29**, 1329 (2008).
8. F. Witte, V. Kaese, H. Haferkamp, E. Switzer, A. Meyer-Lindenberg, C. J. Wirth, and H. Windhagen, *Biomaterials* **26**, 3557 (2005).
9. H. Zreiqat, C. R. Howlett, A. Zannettino, P. Evans, G. Schulze-Tanzil, C. Knabe, and M. Shakibaei, *J. Biomed. Mater. Res.* **62**, 175 (2002).
10. M. P. Staiger, A. M. Pietak, J. Huadmai, and G. Dias, *Biomaterials* **27**, 1728 (2006).
11. B. Heublein, R. Rohde, V. Kaese, M. Niemeyer, W. Hartung, and W. Haverich, *Heart* **89**, 651 (2003).
12. L. Li, J. Gao, and Y. Wang, *Surf. Coat. Tech.* **185**, 92 (2004).
13. C. D. Lee, *Met. Mater. Int.* **8**, 295 (2002).
14. B. S. Shin, Y. Kim, and D. H. Bae, *J. Kor. Inst. Met. & Mater.* **46**, 1 (2008).
15. J. J. Jeon, S. W. Lee, B. H. Kim, B. G. Park, Y. H. Park, and I. M. Park, *J. Kor. Inst. Met. & Mater.* **46**, 304 (2008).
16. G. L. Song, A. Atrens, D. St. John, X. Wu, and J. Nairn, *Corros. Sci.* **39**, 1981 (1997).
17. G. L. Song, A. Atrens, X. Wu, and B. Zhang, *Corros. Sci.* **40**, 1769 (1998).
18. J. D. Hanawalt, C. E. Nelson, and J. A. Peloubet, *Trans. AIME* **147**, 273 (1942).
19. G. L. Song and A. Atrens, *Adv. Eng. Mater.* **1**, 11 (1999).
20. K. N. Reichek, K. J. Clark, and J. E. Hillis, *SAE Technical paper #850417* (1985).
11. R. S. Lillard, *Electrochem. Solid St. Lett.* **6**, B29 (2003).